

# Tracking and validating ICMEs propagating towards Mars using STEREO Heliospheric Imagers combined with Forbush decreases detected by MSL/RAD

Johan L. Freiherr von Forstner<sup>1</sup>, Jingnan Guo<sup>2,1</sup>, Robert F. Wimmer-Schweingruber<sup>1</sup>, Manuela Temmer<sup>3</sup>, Mateja Dumbović<sup>3</sup>, Astrid Veronig<sup>3</sup>, Christian Möstl<sup>4</sup>, Donald M. Hassler<sup>5</sup>, Cary J. Zeitlin<sup>6</sup>, Bent Ehresmann<sup>5</sup>

<sup>1</sup>Institute of Experimental and Applied Physics, University of Kiel, Kiel, Germany

<sup>2</sup>School of Earth and Space Sciences, University of Science and Technology of China, Hefei, China

<sup>3</sup>Institute of Physics, University of Graz, Graz, Austria

<sup>4</sup>Space Research Institute, Austrian Academy of Sciences, Graz, Austria

<sup>5</sup>Southwest Research Institute, Boulder, CO, USA

<sup>6</sup>Leidos, Houston, TX, USA

## Key Points:

- 149 ICMEs propagating towards Mars are studied, combining data from STEREO Heliospheric Imagers with Forbush decreases at MSL/RAD
- 45 ICMEs can be clearly associated with a Forbush decrease at MSL/RAD. Many others are uncertain due to e.g. CME-CME interaction.
- Arrival times predicted from HI data agree with RAD data with a standard deviation of  $\sim 17$  to 19 hours

## Abstract

The Radiation Assessment Detector (RAD) instrument onboard the Mars Science Laboratory (MSL) mission's Curiosity rover has been measuring galactic cosmic rays (GCR) as well as solar energetic particles (SEP) on the surface of Mars for more than 6 years since its landing in August 2012. The observations include a large number of Forbush decreases (FD) caused by interplanetary coronal mass ejections (ICMEs) and/or their associated shocks shielding away part of the GCR particles with their turbulent and enhanced magnetic fields while passing Mars.

This study combines MSL/RAD FD measurements and remote tracking of ICMEs using the STEREO Heliospheric Imager (HI) telescopes in a statistical study for the first time. The large dataset collected by HI makes it possible to analyze 149 ICMEs propagating towards MSL both during its 8-month cruise phase and after its landing on Mars. We link 45 of the events observed at STEREO-HI to their corresponding FDs at MSL/RAD and study the accuracy of the ICME arrival time at Mars predicted from HI data using different methods.

The mean differences between the predicted arrival times and those observed using FDs range from  $-11$  h to  $5$  h for the different methods, with standard deviations between  $17$  and  $20$  hours. These values for predictions at Mars are very similar compared to other locations closer to the Sun, and also comparable to the precision of some other modeling approaches.

---

Corresponding author: Jingnan Guo, [jnguo@ustc.edu.cn](mailto:jnguo@ustc.edu.cn)

## 1 Introduction

Coronal Mass Ejections (CMEs), clouds of magnetized plasma expelled from the Sun, often at high speeds, are one of the main concerns of space weather research. The passage of CMEs at Earth can cause geomagnetic storms (e.g. Cane et al., 2000), which are severe disruptions of the terrestrial magnetic field that can in some cases have serious impact on infrastructure on the surface of Earth, such as damaging electricity grids (Oughton et al., 2017; Boteler et al., 1998). Additionally, shocks driven by fast CMEs are believed to be one of the phenomena responsible for the acceleration of solar energetic particles (SEPs, see e.g. Reames (2013)), which may cause radiation damage to spacecraft, aircraft and astronauts. Consequently, the observation, modeling and, eventually, forecasting of CMEs and their interplanetary counterparts (ICMEs) as well as their impacts on Earth have been important topics in the space weather community in the last decades.

CMEs are usually detected remotely using coronagraph instruments, while their interplanetary counterparts can be observed *in situ* by their signatures in the interplanetary magnetic field, as well as plasma parameters such as the solar wind speed, density and temperature (cf. Zurbuchen & Richardson, 2006). Additionally, ICMEs impact the galactic cosmic ray (GCR) flux in the form of short-term decreases, first observed by Forbush (1937) and Hess and Demmelmair (1937), and later named Forbush decreases (FDs). Since then, numerous authors have studied these effects, which are caused by the magnetic field structure of the ICME and/or its preceding shock shielding parts of the incoming GCR away from the measurement location. The decrease usually takes less than a day while the recovery period of the GCR flux back to its previous level can be much longer (about one week). In the case where both a shock/sheath and the ICME ejecta pass the measurement location, the FD can show a two-step structure, as described by e.g. Cane (2000). FD measurements are suitable for the detection of the arrival time of ICMEs as their onset time usually matches very closely to the corresponding solar wind structure (Cane et al., 1996; Dumbović et al., 2011), and multiple researchers have previously used FDs for this purpose in cases where solar wind and magnetic field measurements are not available (e.g. Möstl et al., 2015; Lefèvre et al., 2016; Vennerstrøm et al., 2016), as was the case at Mars until the MAVEN mission arrived in September 2014 — and even MAVEN does not continuously measure the upstream solar wind due to its elliptic orbit that regularly enters Mars’s magnetosphere. Witasse et al. (2017) have also used Forbush decreases to observe the same ICME at multiple locations in the heliosphere out to 9.9 AU.

Similar decreases in the GCR flux can also be caused by stream interaction regions (SIRs), which are the regions where fast and slow solar wind interact. SIRs often repeat for several solar rotations when the coronal hole structures at the solar surface producing these high speed streams are long-lived (see e.g. Heinemann et al., 2018). These recurrent GCR decreases are also called FDs by some authors, but in this work, we focus on ICME-caused FDs, as we are using them to investigate the propagation of ICMEs.

Considering the increased interest in the exploration of Mars in the recent times, with multiple ongoing robotic missions and plans for human missions in the future, it becomes important to study the effects of radiation and space weather on Mars as well. In our previous work (Freiherr von Forstner et al., 2018), we presented the first statistical studies of ICMEs arriving at Mars, using data from the *Mars Science Laboratory* (MSL) mission’s *Radiation Assessment Detector* (RAD) instrument, which can detect FDs caused by ICMEs passing Mars. The study was based on *in situ* observations of the same ICMEs, first at Earth or one of the STEREO spacecraft (i.e., at a radial distance of about 1 AU from the Sun), and then at Mars (which has a radial distance of about 1.5 AU) yielding the result that most ICMEs in our sample continued to decelerate slightly beyond 1 AU, dragged by the slower surrounding solar wind. The amount of deceleration and the ICME speed relative to the ambient solar wind were also found to have a tendency to correlate, but the statistical significance was limited due to the small num-

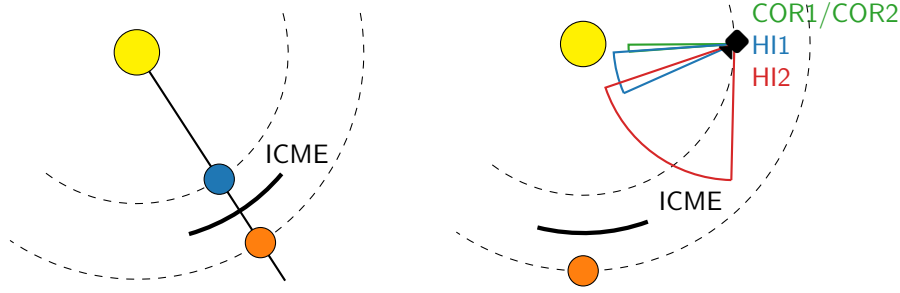


**Figure 1.** Cartoon comparison of the opposition phase constellation to the observation of ICMEs with the STEREO SECCHI instruments. Observations of the same ICME at Earth and Mars are only possible within a small longitudinal separation between the two planets (left, see Freiherr von Forstner et al., 2018), while the STEREO-HI telescopes allow a continuous remote tracking of ICMEs in a wider range of directions (right, this study)

ber of 15 events that could be studied during close alignment of Mars and Earth or STEREO (cf. Figure 1, left panel).

To enable a more complete observation-based study of ICMEs propagating towards Mars, we turn to remote observations in the current study, in particular those made possible by the Heliospheric Imager (HI) telescopes on the STEREO spacecraft. They facilitate tracking of ICMEs all the way from the Sun to approximately 1 AU in a wide range of directions, thus making the study less dependent on a certain constellation of planets and spacecraft (Figure 1, right panel).

In this study, we will combine data from the STEREO-HI instruments with MSL/RAD observations to investigate ICMEs and FDs at Mars in more detail as well as to validate the accuracy of determining the ICME arrival at MSL using STEREO-HI data.

## 2 Data and methods

### 2.1 The MSL/RAD instrument

Since the *Curiosity* rover of NASA’s *Mars Science Laboratory* (MSL) mission (Grotzinger et al., 2012) landed on Mars on August 6, 2012, its *Radiation Assessment Detector* (RAD, Hassler et al., 2012) instrument, built in a cooperation between Kiel University, German Aerospace Center (DLR) and Southwest Research Institute (SwRI), has been continuously measuring the particle radiation environment on the surface of Mars. RAD can detect neutral and charged particles using a setup of 6 detectors, named A through F. For two of the detectors (B and E), the dose rate contributed from all particles observed in the detector is also measured.

The radiation measured on the surface of Mars consists of primary galactic cosmic rays (GCR) and solar energetic particles (SEP) as well as secondary particles created when the primary radiation interacts with the Martian atmosphere (e.g. Guo, Zeitlin, et al., 2018). The daily variation of atmospheric pressure causes a diurnal pattern in the dose rate measured at MSL/RAD (Rafkin et al., 2014). Similar to neutron monitors on Earth and other cosmic ray detectors in deep space, RAD can be used for detecting FDs in the GCR. Due to the larger geometric factor, the dose rate in the E detector, a plastic scintillator, is best used for this purpose. To simplify the detection of FDs in the RAD data, the dose rate measurements are processed using a spectral notch filter described by Guo, Lillis, et al. (2018) to compensate for the diurnal variations.

RAD was also active during most of the time of the MSL rover’s flight from Earth to Mars from December 2011 to July 2012 (the so-called *cruise phase*). Without the Martian atmosphere around it, part of the RAD view cone was only very lightly shielded during this period (Zeitlin et al., 2013) and thus observed a different range of energies in the primary GCR spectrum and a higher number of SEP events. Besides, FDs were also detected during the cruise phase (Guo et al., 2015).

## 2.2 The STEREO Heliospheric Imagers

The Solar TERrestrial RELations Observatory (STEREO) mission (Russell, 2008) was launched in 2006. Its two spacecraft, STEREO A (*Ahead*) and STEREO B (*Behind*) enabled a stereoscopic view of the Sun and inner heliosphere for the first time, with one of the main objectives being the study of CMEs and their impact on Earth. The Sun Earth Connection Coronal and Heliospheric Investigation instrument suite (SECCHI, R. A. Howard et al., 2008) on STEREO consists of multiple telescopes observing the Sun and heliosphere with different fields of view and wavelengths. The Heliospheric Imagers HI1 and HI2 are white-light telescopes and have the largest field of view — combined ranging from  $4^\circ$  to  $88.7^\circ$  on one side of the Sun. This provides an excellent opportunity to observe ICMEs traveling from the Sun outward to 1 AU and beyond.

Connection to the STEREO B spacecraft was lost on October 1, 2014, a few months before its solar conjunction. So after this date, data is only available from STEREO A.

## 2.3 Reconstruction of ICME kinematics from STEREO-HI data

As ICME propagation is a three-dimensional phenomenon, it is not trivial to derive the trajectory from just one (or, for ICMEs seen by both STEREO spacecraft, two) series of 2D images from STEREO-HI. The analysis of HI images is therefore typically based on the identification of ICMEs in J-Map (time-elongation map) diagrams, developed by Sheeley et al. (1999) for the analysis of coronagraph images and applied to STEREO-HI by Rouillard et al. (2008) and Davies et al. (2009), combined with a number of different single-spacecraft fitting or multispacecraft triangulation methods to reconstruct the ICME kinematics.

The time-elongation profile identified in J-Maps is converted to the ICME’s radial distance  $r(t)$  from the Sun based on assumptions about the shape of the ICME and its appearance in the HI images. Different approaches for this conversion can be separated into two types: Single-spacecraft reconstruction methods are based on images from just one of the STEREO spacecraft, while multispacecraft approaches use data from both spacecraft to further constrain the parameters of the ICME trajectory (e.g. Liu, Davies, et al., 2010; Liu, Thernisien, et al., 2010; Lugaz et al., 2010a).

These multispacecraft triangulation methods have been used to study many ICMEs propagating towards Earth, and they make it possible to relax some of the assumptions that need to be made when using only single-spacecraft methods. This allows for a detailed study of the ICME’s speed profile within the HI field of view (e.g. Liu et al., 2013, 2016). However, the orbits of the STEREO spacecraft are optimized for observing Earth-directed structures and thus multi-spacecraft HI observations are often not possible for ICMEs propagating towards Mars. Also, our study includes some events after 2014, where only STEREO A is available. Therefore, we will focus on the most common single-spacecraft methods here, which are shown in Figure 2.

One of the simplest single-spacecraft reconstruction methods is the Point-P method (PP, T. A. Howard et al., 2006), where the ICME is regarded as an expanding circular front centered around the Sun. On the contrary, the Fixed- $\phi$  model (FP, Sheeley et al., 1999; Kahler & Webb, 2007) reduces the shape of the ICME to a single point moving away from the Sun radially with a fixed longitudinal separation  $\phi$  from the observer. The

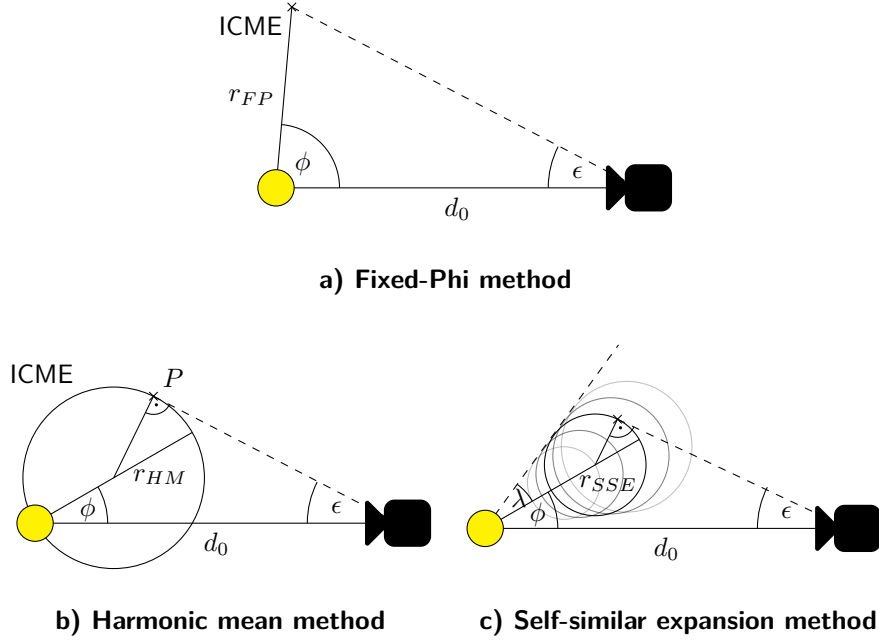


**Figure 2.** Single-spacecraft reconstruction methods for Heliospheric Imaging observations: a) Fixed  $\phi$  (Kahler & Webb, 2007), b) Harmonic mean (Lugaz, Vourlidas, & Roussev, 2009), and c) Self-similar expansion (Davies et al., 2012; Lugaz et al., 2010b).

Harmonic Mean method (HM, Lugaz, Vourlidas, & Roussev, 2009) is a middle ground between these two extremes, where the circular ICME has one edge fixed at the Sun instead of being centered around it, which is equivalent to calculating the harmonic mean of the PP and FP results. Appendix B of (Liu, Thernisien, et al., 2010) contains a more detailed description of these three methods.

Finally, the more recent Self-similar-expansion method (SSE, Davies et al., 2012; Lugaz et al., 2010b) introduces a second parameter  $\lambda$  for the half-width of the ICME, which can be seamlessly adjusted between the two edge cases for  $\lambda = 90^\circ$  ( $\Rightarrow$  HM) and  $\lambda = 0^\circ$  ( $\Rightarrow$  FP).

The FP, HM and SSE methods are usually combined with fitting algorithms (FPF, HMF and SSEF) to determine parameters such as the longitudinal propagation direction of the CME under the assumption of a constant speed. As the leading edge of the visible structure is marked in the J-Map,  $r(t)$  and the resulting speed  $v$  are believed to most likely correspond to the shock front, if present, and otherwise the front of the ICME ejecta.

## 2.4 The HELCATS catalogs

On its website at <https://www.helcats-fp7.eu>, the *Heliospheric Cataloguing, Analysis and Techniques Service* EU project (HELCATS, Helcats et al., 2018) has collected a large number of ICMEs observed with the STEREO-HI instruments. Their *HIGeoCat* CME kinematics catalog (version 5) contains 1459 ICMEs, each one supplemented with the associated J-Map and a time-elongation profile extracted from it by manual selection. Results for ICME speeds and propagation directions derived using the FPF, HMF and SSEF methods are also provided (under the assumption of a constant speed  $v$ , longitude  $\phi$ , and in the SSE case, a fixed half-width of  $\lambda = 30^\circ$ ).

The *ARRCAT* arrival catalog contains a list of predicted *in situ* arrival times of ICMEs at different planets and spacecraft including MSL, based on the events in the *HI-GeoCat* and currently (version 01) updated until the end of September 2014, where STEREO B data ends. As described by Möstl et al. (2017), the arrival time predictions were calculated based on the SSEF30 method results from HIGeoCat, extrapolating the trajectory up to the respective location based on the constant speed  $v$ . The calculation also includes the correction described by Möstl and Davies (2013) to account for the SSE geometry at locations that are not directly hit by the ICME apex.

Möstl et al. (2017) also compared the ARRCAT data for multiple locations in the inner heliosphere with *in situ* plasma and magnetic field data to check the accuracy of the predicted arrival times. However, their study does not include MSL or other spacecraft at Mars.

### 3 Results and Discussion

#### 3.1 ICMEs observed by STEREO-HI and their arrival times at MSL/RAD

To analyse ICMEs that arrived at MSL, we first select candidate events from the HELCATS HIGeoCat by requiring the propagation direction (heliospheric longitude, determined using the SSEF30 method) to be within  $\pm 30^\circ$  of MSL's longitude at that time. Although the longitude depends considerably on the geometry used for fitting the HI data (Lugaz, Vourlidas, Roussev, & Morgan, 2009; Liu et al., 2013, 2016), we use the modeled direction from SSE as it is the most advanced of the three methods available in the HIGeoCat. Also, this selection criterion is equivalent to the one used for the HELCATS ARRCAT catalog and the corresponding paper by Möstl et al. (2017), making it possible to compare to their results afterwards (see Section 3.2). The selection yields 149 ICME events between the beginning of MSL's cruise phase in November 2011 and the current end of the HIGeoCat catalog (version 5) in November 2017. 31 of these events were observed with both STEREO spacecraft according to the HELCATS HIJoinCat catalog, the remaining 118 ICMEs were only detected by one of them. For events where observations from both spacecraft were available, we use the spacecraft data which predict an arrival at MSL based on the SSEF30 fitting. If both STEREO observations predict the ICME to arrive at MSL, we use STEREO A data as a preference.

A plot showing the time distribution of the 149 events is displayed in Figure 3. It can easily be seen that the ICMEs are not evenly distributed, but rather concentrated into three discrete periods. The reason for this is that in contrast to the coronagraph instruments, the heliospheric imagers' fields of view are limited to one side of the Sun, and the STEREO spacecraft are always pointed in a way that the side of the Sun at which HI looking is the one where Earth is located. So when e.g. Earth is on the right side of the Sun as seen from one of the STEREO spacecraft while Mars is on the left side, ICMEs propagating towards Mars cannot be seen using the HI instruments on this spacecraft. The last period in 2016–17 has fewer events, which is related to the solar cycle approaching its minimum as well as the loss of STEREO B data since 2014.

For each of the 149 events, a plot similar to Figure 4 was constructed, showing time series of the ICME's radial distance from the Sun, which were derived using the SSE geometry and the longitude derived from the SSEF30 method results (panel b)), the longitudinal separation between the CME apex and MSL's location (panel a)) as well as the MSL/RAD dose rate processed using the notch filter described in Section 2.1 (panel c)). The time-distance plot was corrected based on the longitudinal separation between the ICME apex and MSL using the equation from Möstl and Davies (2013) so that it shows the radial distance of the part of the ICME in the SSE geometry that hits MSL, therefore resulting in a slightly lower speed. The predicted ICME arrival time at MSL



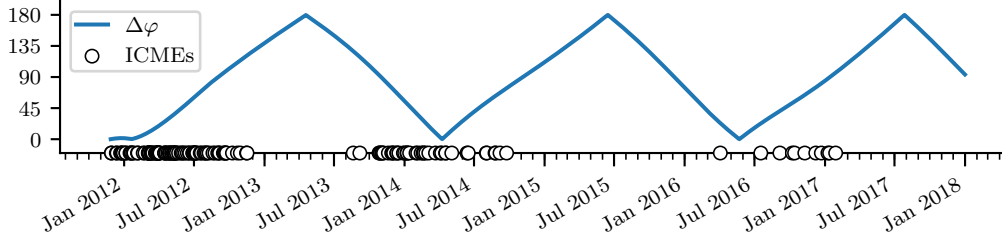


**Figure 3.** Time distribution of the 149 ICMEs propagating towards MSL  $\pm 30^\circ$  from the HELCATS catalog, plotted together with the longitudinal separation  $\Delta\varphi$  between Earth and MSL. During periods with large  $\Delta\varphi$ , STEREO-HI cannot see ICMEs propagating towards MSL, as it is only looking at one side of the Sun.

could then be calculated based on the  $r(t)$  trajectory and was marked with a vertical line in both the  $r(t)$  and RAD dose rate panels.

It needs to be stated that these “predictions” were done on the basis of post-event analysis using science data and not real-time beacon data. However, as ICMEs are usually only visible in HI images up to about 1 AU or less, the predictions at Mars are probably comparable to what could have been done with real time data in most cases — in contrast to the ARRCAT predictions at locations closer to the Sun (Möstl et al., 2017), which are partly based on observations that would only have been available after the ICME arrival. A study using real time STEREO-HI data was conducted by Tucker-Hood et al. (2015).

Based on the predicted arrival time at MSL/RAD, a corresponding FD in the MSL/RAD data was searched for. In general, we used a time window of at most  $\pm 2.5$  day around the predicted arrival time to make sure that the FD onset time was not too far off and thus maybe related to a completely different event. We also took care that series of events predicted to arrive in a certain order were matched to the FDs in the correct sequence if no interaction between the ICMEs is predicted, and that for CMEs also seen at Earth close to oppositions of MSL and Earth, the arrival at Mars is not earlier than the one at Earth. Although the time window might seem quite small for slow CMEs, a larger window would have caused more ambiguous cases with multiple candidate FDs.

The FD onset was marked to be the point in time where the GCR intensity reaches its maximum at the beginning of the FD. This makes the onset time a more well-defined quantity compared to just marking it “by eye”, and was implemented by searching for the maximum within a  $\pm 4$  h window around the onset time that was first manually selected.

In the process of marking the FD onset times, the 149 ICMEs were sorted into five categories, by looking at the RAD data as well as the ICME trajectories calculated from HI data and their extrapolations:

1. Events with a clearly identifiable FD at MSL — **40 ICMEs**
2. ICMEs that might have interacted with others on their way to MSL, but still have a clear correspondance to a FD at Mars (either completely separate or multiple steps) — **5 ICMEs**
3. ICMEs that probably interacted with others on their way to MSL, so that their FDs can not be matched unambiguously (e.g. because there is only one merged FD or none at all) at MSL — **53 ICMEs**

**Table 1.** Table of all 45 events where an arrival time at Mars could be determined (categories 1 and 2 from Section 3.1). The first two columns show the IDs of the ICMEs in the HELCATS catalog for STEREO A and B observations, which also correspond to the date where the ICME was first observed in HI images, and the third column shows the STEREO spacecraft that was used for applying the fitting methods. The fourth and sixth column show the longitude  $\phi$  and the speed  $v$  of the ICME as determined by the HELCATS project using the SSEF30 method. Additional columns show the differences between  $\phi$  and the heliospheric longitudes of the respective STEREO spacecraft (column 5) or MSL (column 7) at that time as well as the *in situ* arrival time (Forbush decrease onset) at MSL and the transit time  $T_{\text{MSL}}$  between the launch at the Sun and arrival at MSL. The arrival time and longitudinal separation are also given for the arrival at Earth, if applicable.

ICME-A.....	ICME-B.....	SC	$\phi_{\text{SSEF30}} / ^\circ$	$\Delta\phi_{\text{STEREO}} / ^\circ$	$v_{\text{SSEF30}} / \text{km s}^{-1}$	$\Delta\phi_{\text{MSL}} / ^\circ$	$t_{\text{MSL}}$	$T_{\text{MSL}}/d$	$\Delta\phi_{\text{Earth}} / ^\circ$	$t_{\text{Earth}}$
2011211.01	2011211.01	A	3	-27	452	-28.7	2011-12-17 01	5.8	-27	
2011222.01	2011222.01	A	221	-24	320	-25.3	2011-12-28 08	6.1	-24	
	2011226.01	B	206	15	686	13.7	2011-12-30 01	3.7	15	
2012023.01	2012023.01	A	207	20	1052	20.4	2012-01-24 21	1.9	20	
	2012024.01	B	100	-25	885	-17.6	2012-02-27 08	3.2	-25	2012-02-26 23
20120310.01	20120310.01	A	266	-14	1447	-1.9	2012-03-12 21	2.3	-14	2012-03-12 02
20120322.01	20120322.01	A	127	-3	469	13.1	2012-03-28 11	6.5	-3	2012-03-26 20
20120415.01	20120415.02	B	133	-39	316	-13.4	2012-04-21 02	5.9	-39	
	20120512.01	B	159	-19	869	17.9	2012-05-15 12	3.6	-19	2012-05-15 00
20120630.01	20120702.01	A	261	-30	686	15.5	2012-06-03 04	3.6	-30	2012-06-02 07
	20120702.02	B	163	-55	697	6.2	2012-07-06 07	4	-55	
	20120915.01	B	173	-44	398	17.4	2012-07-09 10	7	-44	
	20120915.02	B	223	-85	441	11	2012-09-21 17	6.5	-85	
	20120918.01	B	193	-84	412	13.1	2012-09-23 14	6.1	-84	
	20120920.01	B	141	-99	528	-1.6	2012-09-25 09	5.2	-99	
	20120922.01	B	111	-111	562	-13	2012-09-27 01	5.5	-111	
	20120923.01	B	121	-78	620	21.5	2012-09-28 10	5	-78	
	20121022.01	B	92	-95	427	16.3	2012-10-27 08	5.7	-95	
	20121029.01	B	357	-89	342	24.6	2012-11-05 16	7.5	-89	
	20121115.01	B	127	-110	349	10.3	2012-11-20 19	6.7	-110	
	20121116.01	B	108	-105	534	15.5	2012-11-20 06	4.4	-105	
	20130820.01	A	263	105	701	-22.5	2013-08-24 22	5.1	105	
20131119.01	20131119.01	A	87	55	577	-24.4	2013-11-25 01	5.8	55	
2014001.01	2014001.01	A	249	58	311	2.4	2014-01-10 11	9.7	58	
20140114.01	20140114.01	A	65	46	655	-1.3	2014-01-18 09	4.5	46	
20140204.01	20140204.01	A	197	37	451	-0.6	2014-02-06 18	7.2	37	2014-02-05 18
20140213.01	20140213.01	A	111	9	832	-26.1	2014-02-08 14	4.7	9	2014-02-07 20
20140220.01	20140220.01	A	298	50	763	28	2014-02-17 06	4.4	58	2014-02-15 13
20140225.01	20140225.01	A	198	13	661	-10.2	2014-02-24 04	4	50	2014-02-23 14
20140322.01	20140322.01	A	244	34	798	-10.2	2014-03-01 10	4.5	13	2014-02-28 02
20140404.01	20140404.01	A	54	9	895	24.9	2014-03-26 22	4.6	34	
	20140407.01	B	335	-26	535	-26.5	2014-04-06 16	2.8	9	2014-04-05 11
20140418.01	20140418.01	A	218	-3	1265	1.8	2014-04-14 04	7	-26	2014-04-11 16
20140504.01	20140504.01	A	235	22	1092	27.1	2014-04-20 16	2.8	-3	2014-04-20 09
	20140801.01	B	237	-24	754	16.9	2014-04-22 02	3.7	22	2014-04-20 17
	20140803.01	B	218	-26	790	27.7	2014-04-22 02	3.7	22	
	20140923.02	B	178	-102	754	-28	2014-08-04 23	3.3	-24	
		B	132	0	751	-23.2	2014-08-06 20	3.9	-26	
20160403.01	20160403.01	A	112	-56	478	-3.5	2016-04-06 05	4.7	-102	
20161007.01	20161007.01	A	32	-64	345	-9.3	2016-10-12 14	4.9	-56	
20161013.01	20161013.01	A	15	-90	314	-26.7	2016-10-19 15	6.5	-64	
20161027.01	20161027.01	A	23	-63	381	12	2016-11-17 17	9.1	-90	
20161222.01	20161222.01	A	187	-67	330	12.9	2016-12-14 14	7.1	-63	
							2016-12-29 12	7.5	-67	



4. Other events that don't show a clear FD at Mars (either the FD is too weak or the ICME missed MSL completely) — **19 ICMEs**
5. Events where the analysis could not be applied due to a data gap or an SEP event at MSL/RAD coinciding with the FD, or poor visibility in the STEREO-HI image leading to a high uncertainty of the predicted arrival time — **32 ICMEs**

This categorization shows that for all 117 events where the HI and RAD data quality is sufficient (excluding category 5), 45 are clearly identifiable. So, based on the results for our sample, there is a  $(39 \pm 6)\%$  chance that an ICME observed in STEREO-HI and predicted to arrive at MSL by the SSEF30 method data is actually observed through a FD at MSL/RAD that is clearly related to the ICME. This is consistent with the performances between 12 % and 44 % for different locations in the inner heliosphere found by Möstl et al. (2017, see their Table 1).

In  $(50 \pm 8)\%$  of the cases, multiple ICMEs interacted and possibly merged, making it impossible to unambiguously match the FD to a single ICME (Category 3). When only considering the 59 individual ICMEs with no others occurring in quick succession and similar direction (Categories 1 and 4), the chance that a clearly related FD is observed at Mars grows to  $(68 \pm 14)\%$ . The uncertainties of the percentages given here were calculated assuming Poisson statistics ( $\sigma = \sqrt{N}$ ).

Only the events in categories 1 and 2 will be used in the following studies, as these are the only ones where an arrival time at MSL could be defined. A list of these events with the relevant SSE fit results and FD onset times can be found in Table 1.

14 of these 45 ICMEs were close to oppositions of Earth and Mars (cf. Figure 1, left panel) and thus were also seen at Earth. In these cases, we also included the arrival times at Earth, which were derived in a similar fashion based on Forbush decreases in data from the South Pole neutron monitor. We have also done a basic comparison of arrival times at Earth with visible shock and/or ICME structures in solar wind and magnetic field measurements from ACE, and found that the Forbush decrease onsets agree reasonably well (usually within  $\sim \pm 2$  h) with this data.

### 3.2 Comparison of FD results with STEREO-HI predictions

For the 45 events where a clear FD at Mars was found (see Table 1), we compared the measured FD onset times to the predicted arrival times using the three single-spacecraft fitting methods used in the HELCATS catalog. Figure 5 shows histograms of the time difference  $\Delta t = t_{\text{calculated}} - t_{\text{observed}}$  for each of the three methods with two approaches.

First, the upper panels of Figure 5 show the results from the original techniques (summarized by Möstl et al., 2014), which assume a constant speed and direction to calculate the CME arrival times at Mars. They are based on the CME speed and launch times in the HELCATS HIGeoCAT catalog and we take into account the appropriate correction equations for the circular CME front shapes in the HM and SSE geometries (see Möstl et al., 2011; Möstl & Davies, 2013). This is similar to the aforementioned ARRCAT for SSEF, but here we also include the FPF and HMF methods.

Secondly, in the lower three panels, results on the differences between calculated and observed arrival times are presented which were generated with an extrapolation method. Here, we do not assume a constant CME speed over the whole HI field of view, but instead only for an interval over the last 10 available HI data points, allowing an acceleration or deceleration before this time. The physical reason behind this assumption is that CMEs decelerate or accelerate closer to the Sun and eventually reach an equilibrium with the background solar wind (e.g. Liu et al., 2013). For the larger heliocentric distances of Mars compared to the inner planets, an assumption of constant speed over the full HI field of view may lead to systematic shifts in the predicted arrival times. To this end,

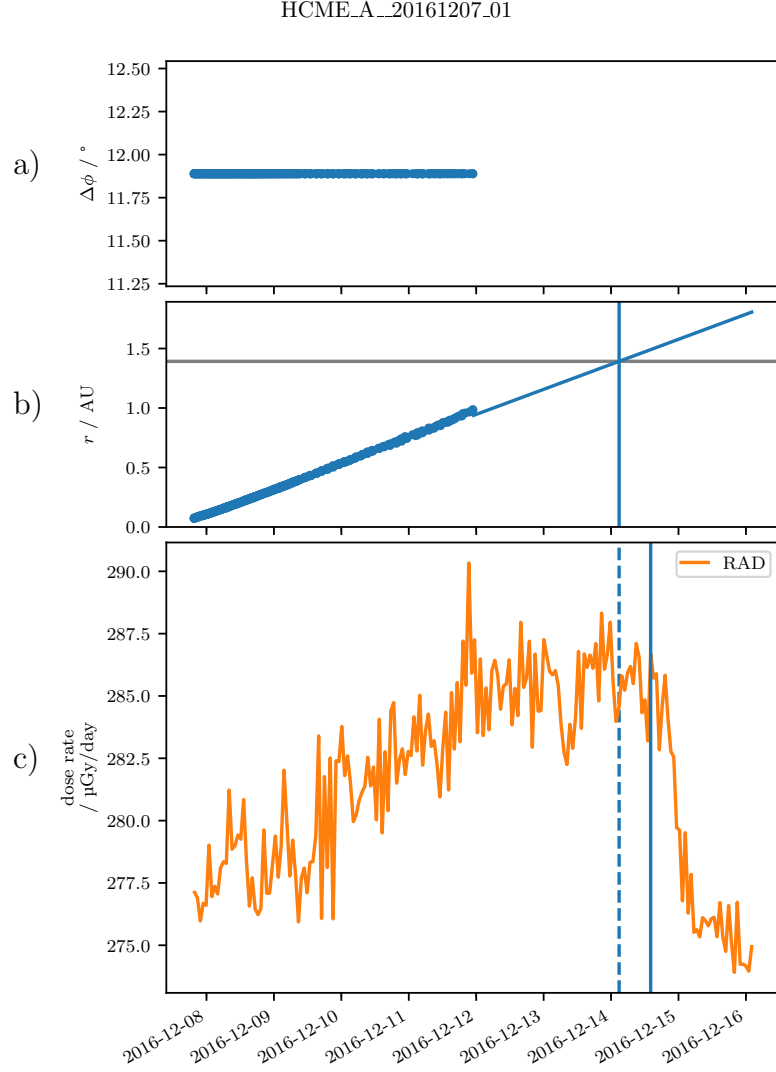


**Figure 4.** An example of the type of plot used to compare the ICME arrival times at Mars that were predicted using STEREO-HI observations and the onset time of the corresponding FD detected at MSL/RAD. This plot is for the “HCME\_A\_20161207.01” event from the HELCATS catalog. Panel c) shows the MSL/RAD dose rate measurements where the FD onset is marked with a solid blue line. In panel b), the trajectory of the ICME in the direction of MSL (radial distance from the Sun over time) is plotted, which was calculated from the time-elongation data using the SSEF30 method and then extrapolated assuming the launch time and the constant speed that result from the SSEF30 fitting procedure. The blue vertical line in this panel marks the time where the extrapolation intersects Mars’s radial distance from the Sun, i.e. the predicted arrival time at Mars, and this line was extended into panel c) as a dashed line. Panel a) shows the longitudinal separation between Mars and the ICME apex (in this case constant, because it is determined from the SSEF30 fit).

for each event an  $r(t)$  kinematic is created by the FP, HM and SSE conversion methods for elongation to distance, including the correction formulae for HMF and SSEF, and a linear fit was applied to the 10 points farthest from the Sun. The arrival time of the CME is then taken as the time where the linear fit intersects the current radial distance of Mars from the Sun.

Note that this second method is not fully self-consistent. In order to derive  $r(t)$  we need a CME direction, and the direction from single-spacecraft fitting was determined with the assumption of constant speed. Also, the uncertainty in the elongation value of the last 10 points may be larger due to the CME appearing more faint in the HI images as it expands. This extrapolation method should thus be seen as a first step towards allowing a variation of the CME speed with HI fitting methods (elaborated by Tucker-Hood et al., 2015; Rollett et al., 2016; Amerstorfer et al., 2018), but needs to be taken with a grain of salt due to the abovementioned issues.

Comparing the Fixed- $\phi$ , Harmonic Mean and SSE methods as shown in Figure 5, all perform similarly well in predicting the arrival times, with FPF and HMF (panels a) and b)) giving a slightly earlier arrival ( $\Delta t < 0$ ) and SSEF (panel c)) a slightly later arrival ( $\Delta t > 0$ ) on average. The standard deviations are also similar for all three methods, they all fall into the 17 h to 20 h range. The extrapolation method in panels d), e), and f) also leads to almost similar results as the original fitting techniques.

Our result for SSE with the assumption of a constant speed ( $\Delta t = (4.4 \pm 18.1)$  h, panel c)) is also very similar to the values obtained by Möstl et al. (2017, their Table 1) for arrival time predictions at other locations in the heliosphere: Their results lie between  $-2.1$  h and  $8.0$  h for the average  $\Delta t$  and between  $12.9$  h and  $23.4$  h for its standard deviation. It is interesting that there seems to be no clear dependence of the prediction accuracy (neither for the average value nor its standard deviation) on the distance from the Sun, even though one would intuitively think that the uncertainty should increase with greater distance as errors in the model accumulate. However, at least up to Mars ( $\sim 1.5$  AU), this dependence is probably not significant compared to the inherent uncertainty coming from the strong geometric and kinematic assumptions of the method. This might change with new models such as the ElEvoHI method (Rollett et al., 2016), which relaxes the assumption of a constant speed and also allows the ICME front to have an elliptical shape instead of being necessarily circular. The inclusion of a drag-based model (Vršnak et al., 2013) for the speed evolution is especially important — the assumption of a constant speed in most previous models is very often not true due to the interaction of ICMEs with the surrounding solar wind (as shown by many previous studies, including Vršnak & Žic, 2007; Freiherr von Forstner et al., 2018; Witasse et al., 2017) as well as other heliospheric structures such as stream interaction regions and other ICMEs, with which the ICME can collide (Temmer et al., 2012; Temmer & Nitta, 2015; Shen et al., 2012; Guo, Dumbovi, et al., 2018). The ElEvoHI implementation is currently still under development and has not yet been applied automatically to large datasets such as the HELCATS catalog. Amerstorfer et al. (2018) have applied ElEvoHI ensemble modeling to a case study of one event and were able to constrain the uncertainties to less than  $\pm 2$  h, which is a very promising result.

To find out to what extent the differences in average values as well as standard deviations for  $\Delta t$  between the different models are significant, we estimated the statistical error of the mean and standard deviation by fitting a Gaussian profile to the histogram results from Figure 5, which can also be seen in the same figure. The standard deviations for both parameters  $\sigma$  and  $x_0$ , calculated as the square root of the covariance matrix's diagonal, lie in the  $0.8$  h to  $2.3$  h range — so in fact, one could argue that at least with respect to the standard deviation of  $\Delta t$ , all single-spacecraft methods perform almost equally well on average, only the systematic offset ( $\bar{\Delta t}$ ) changes depending on the method, similar to what was previously found by Möstl et al. (2014) for ICMEs arriving at 1 AU.

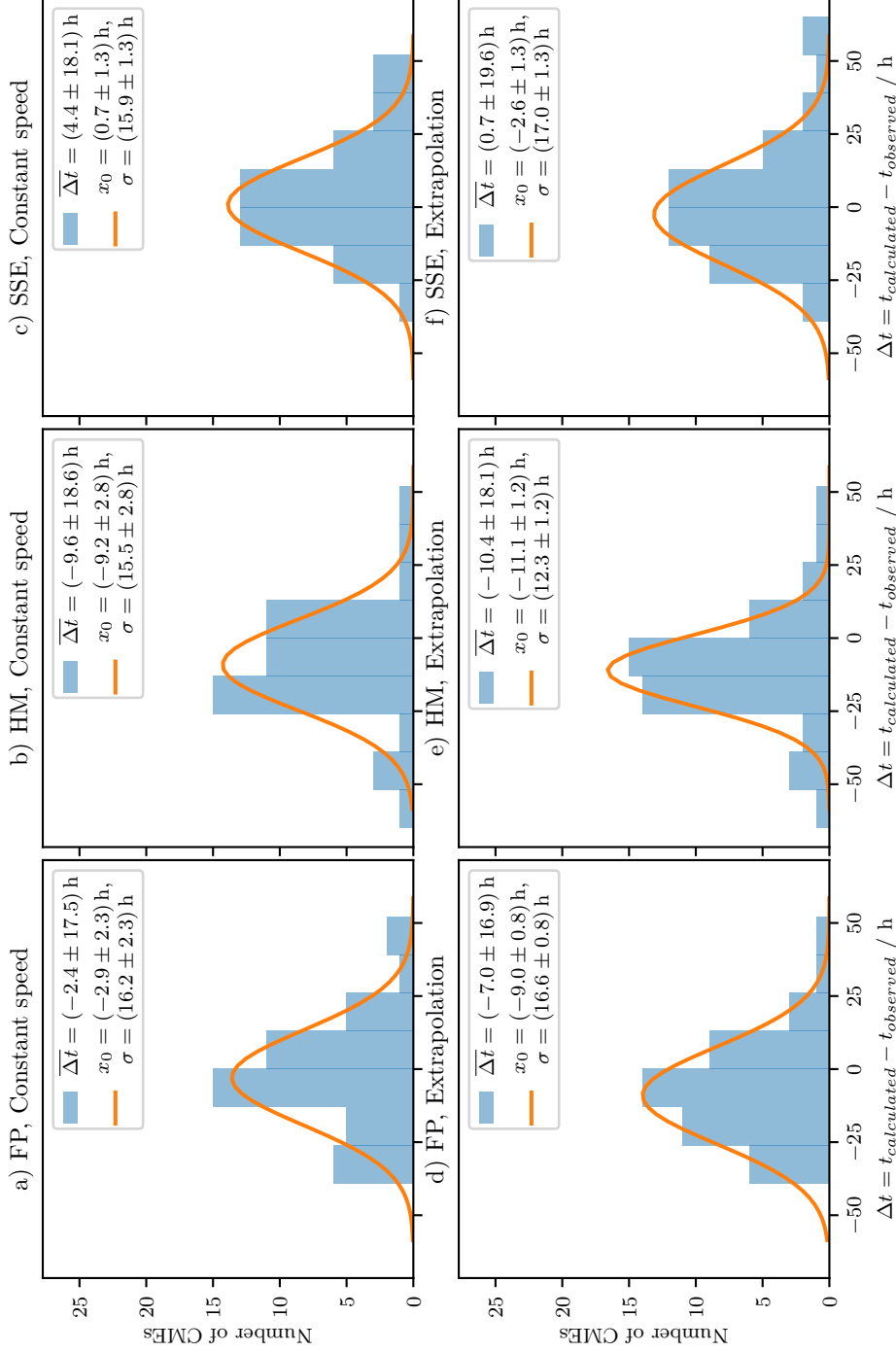


**Figure 5.** Comparison of arrival times predicted using STEREO-HI tracking with the FP, HM and SSE methods to actual FD onset times measured at MSL/RAD.  $\Delta t < 0$  or  $\Delta t > 0$  corresponds to an earlier/late predicted arrival compared to the FD onset. The top three panels use the fitting results assuming a constant speed throughout the HI field of view, the lower panels extrapolate the results using a line fitted to the last 10 points of the  $r(t)$  trajectory. All panels have the same x and y axis scaling as well as the same histogram bins. Additionally, a Gaussian distribution fitted to the histograms is displayed. The legends show both the results for the mean and standard deviation of  $\Delta t$  calculated directly from the distribution as well as the parameters  $x_0$  and  $\sigma$  obtained from the Gaussian fit.

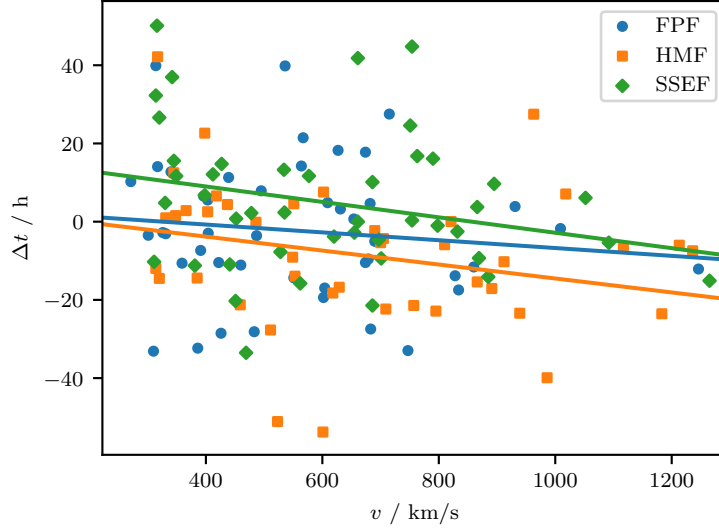


**Figure 6.** Plot of the dependence of the difference  $\Delta t$  between the predicted and observed arrival times on the speed of the ICME for the three fitting methods FPF, HMF and SSEF.  $\Delta t < 0$  or  $\Delta t > 0$  corresponds to an earlier/later predicted arrival compared to the FD onset. Each of the three sets of points is supplemented with a linear regression to show the general trend. The slopes of the three lines are:  $(-0.010 \pm 0.013) \text{ h km}^{-1} \text{ s}$  (FPF),  $(-0.018 \pm 0.008) \text{ h km}^{-1} \text{ s}$  (HMF),  $(-0.020 \pm 0.010) \text{ h km}^{-1} \text{ s}$  (SSEF). If we fit all three sets of points together with one line to reduce the uncertainty, we obtain a slope of  $(-0.019 \pm 0.005) \text{ h km}^{-1} \text{ s}$ .

Another way to look at the predicted and observed arrival times is shown in Figure 6, where  $\Delta t$  is plotted against the speed of the ICME. The plot suggests that there is a trend to predicting an earlier arrival for fast ICMEs ( $\Delta t < 0$ ) and a later arrival for slow ICMEs ( $\Delta t > 0$ ), i.e. the speed of fast ICMEs is overestimated and the speed of slow ICMEs is underestimated. This is supported by the linear fits shown in the figure, which have a negative slope. Intuitively, this can be explained as being related to the assumption of a constant speed in the three fitting methods — A fast ICME usually decelerates due to the slower surrounding solar wind, but when a constant speed is assumed, the predicted arrival will be earlier. This trend may be slightly less pronounced for FPF than for the other two methods, but in all three cases, the scatter of the data points is significant.

The accuracy of the three different geometric methods can also depend on the longitudinal separation  $\Delta\phi$  of the ICME and the observing STEREO spacecraft (which is also shown in Table 1). For example, when applying the FP method to an event with a large longitudinal separation, the geometry can lead to a perceived acceleration of an ICME at larger radial distances, which is often not physical (Liu et al., 2013, 2016). However, this does not directly apply to the FPF, HMS and SSEF fitting methods, as in this case,  $\Delta\phi$  is not pre-defined, but rather a result of the fitting method and therefore differs between the three methods. For this reason, we have not found a clear trend for the dependence of the prediction accuracy on the longitudinal separation.

The predicted arrival time uncertainties found here with a standard deviation of 17 h to 20 h for the three geometric models are similar to those obtained via some other approaches of modelling ICME propagation, such as the magnetohydrodynamic WSA-ENLIL+Cone model (Odstrcil et al., 2004) as well as the analytical Drag-Based Model

(Vršnak et al., 2013). For example, Vršnak et al. (2014), who applied both models to a sample of 50 ICMEs arriving at Earth, found a standard deviation of 16.9 h for ENLIL and 18.3 h to 19.1 h for DBM. A more recent study by Dumbovi et al. (2018) using a different sample of 25 events and the ensemble modeling versions of ENLIL and DBM found the standard deviations to be slightly lower at 14.4 h for ENLIL and 16.7 h for DBM. For arrivals at Mars, these standard deviations are expected to increase slightly more, as the uncertainties of the models accumulate because no measurements further away from the Sun are used to constrain the simulation. Freiherr von Forstner et al. (2018) only found a standard deviation of 11 h between ENLIL results and measurements, but the set of events was much smaller and carefully chosen, and the simulation input parameters were additionally validated using the measurement at 1 AU, so this is not directly comparable. Dumbovi et al. (2018) also found the prediction accuracy of DBEM to be dependent on the CME speed, where fast CMEs are predicted to arrive earlier than observed — similarly to our STEREO-HI results.

This implies that the forecasting accuracy is very similar for the different fitting methods based on STEREO-HI data and simulations using DBM or ENLIL. Specifically speaking, DBM and ENLIL contain a more sophisticated description of the ICME kinematics and its interaction with the solar wind, but their initial parameters are only based on observations close to the Sun. STEREO-HI, on the other hand, is a direct observation much further out into the heliosphere, but the simple reconstruction methods based on single-spacecraft observations need to make strong assumptions on the ICME geometry and kinematics.

In Freiherr von Forstner et al. (2018), we also applied a different method of forecasting the arrival time at Mars by using the in situ measurement at 1 AU as the inner boundary condition for the DBM model, yielding a higher accuracy. However, this method is only applicable when in situ measurements are available at multiple locations preferentially radially aligned. Such observations are unfortunately rather limited and often taken from planetary missions which are not optimized for studying heliospheric physics (Witasse et al., 2017; Winslow et al., 2018; Wang et al., 2018). In the future, with more data from Parker Solar Probe and Solar Orbiter, we hope to have improved space weather forecasts based on modeling of CME propagations constrained by in situ measurements.

## 4 Conclusions and Outlook

In this work, we studied 149 ICMEs propagating towards Mars (between August 2012 and February 2017) as well as towards the MSL spacecraft during its flight to Mars (between December 2011 and July 2012). These events were observed remotely with the Heliospheric Imagers onboard the STEREO spacecraft as well as *in situ* at their arrival through FDs measured with MSL/RAD. Links were established between the remote and in situ observations, with a  $(39 \pm 6)\%$  chance that an ICME that is headed for  $\text{MSL} \pm 30^\circ$  according to the SSE model corresponds to a clear FD observed at RAD. This can be seen as a measure of the SSE model’s performance for predictions of ICME arrivals at MSL’s location using FDs as the method of identification of the arrival. In  $(50 \pm 8)\%$  of cases, there was likely interaction between multiple ICMEs — when excluding these, the chance of a clear and distinguishable FD grows to  $(68 \pm 14)\%$ .

For the 45 remaining ICMEs where a clear FD could be observed at MSL/RAD, we could also measure the accuracy for predicting the arrival time of the ICME using the SSE, Fixed- $\phi$  and harmonic mean geometries. The average  $\Delta t$  varies between  $-10.4$  h and  $4.4$  h, while the standard deviations are all very similar between  $16.9$  h and  $19.6$  h. The results for the SSE method —  $\Delta t = (4.4 \pm 18.1)$  h — are very comparable to the values that Möstl et al. (2017) found for arrivals at different locations in the inner heliosphere.



These standard deviations are also similar to the performance of most other current ICME modelling approaches, such as the WSA-ENLIL+Cone model and the Drag-Based Model. In the future, better results can probably be obtained with more physical and realistic geometric models applied to heliospheric imager data, such as the ElEvoHI method (Rollett et al., 2016) as well as new state-of-the-art MHD simulations such as the recently developed EUHFORIA model (Pomoell, Jens & Poedts, S., 2018). Certainly, more multi-point HI observations would also be helpful, which are currently not possible as data from STEREO B is not available. Future missions carrying heliospheric imagers include NASA’s recently-launched Parker Solar Probe (Fox et al., 2016) with its WISPR instrument (Vourlidas et al., 2016), ESA’s Solar Orbiter mission (Müller et al., 2013) currently scheduled to launch in 2020 with its SoloHI (R. A. Howard et al., 2013), as well as a possible future mission to the L5 Lagrange point (proposed by e.g. Gopalswamy et al., 2011; Vourlidas, 2015; Lavraud et al., 2016; Kraft et al., 2017).

In a future study, we plan to use the catalog of ICMEs at Mars built in this work to investigate the properties of the Forbush decreases, such as their magnitude and steepness, in more detail. For the 14 events seen at both Earth and Mars, we will also directly compare these data at the two planets for better understanding their properties and interplanetary propagations. For up to about 6 events from this catalog, the ICME and Forbush decrease properties can be better studied by also taking into account in situ measurements of solar wind and magnetic field from the MAVEN spacecraft that arrived at Mars in late 2014. However, MAVEN can only measure the upstream solar wind intermittently due to the spacecraft orbit (as discussed in the Introduction), resulting in frequent gaps in the data.

Nevertheless, our current results are important for the understanding of space weather, but of course also for the development of future deep space missions and human spaceflight to Mars, where accurate predictions of ICMEs, their associated shocks and accompanying SEP events, and their impact are essential.

## 5 Sources of Data and Supplementary Material

This section includes references to all the data used in this work.

The **HELCATS** catalogs are available from the HELCATS website, <https://www.helcats-fp7.eu>:

HIGeoCat: <https://doi.org/10.6084/m9.figshare.5803176.v1>

HIJoinCat: [https://www.helcats-fp7.eu/catalogues/wp2\\_joincat.html](https://www.helcats-fp7.eu/catalogues/wp2_joincat.html)

ARRCAT: <https://doi.org/10.6084/m9.figshare.4588324>

**RAD** data are archived in the NASA planetary data systems planetary plasma interactions node (<http://ppi.pds.nasa.gov/>). Other file formats can be provided by the authors on request.

**South Pole neutron monitor** data can be retrieved from the Neutron Monitor Database at <http://nmdb.eu>.

A text file version of Table 1 in this work can be found on FigShare at <https://doi.org/10.6084/m9.figshare.7440245>.

## Acknowledgements

J. v. F. thanks Joana Wanger, who helped with the task of marking FD onset times in the MSL/RAD data during her internship in the Extraterrestrial Physics group at Kiel University.

C. M. thanks the Austrian Science Fund (FWF): [P26174-N27].

M. T. acknowledges the support by the FFG/ASAP Programme under grant no. 859729 (SWAMI).

M. D. acknowledges funding from the EU H2020 MSCA grant agreement No 745782 (project ForbMod).

J. G. is partly supported by the Key Research Program of the Chinese Academy of Sciences under grant no. XDPB11.

RAD is supported by NASA (HEOMD) under JPL subcontract 1273039 to Southwest Research Institute and in Germany by DLR and DLR's Space Administration grants 50QM0501, 50QM1201, and 50QM1701 to the Christian Albrechts University, Kiel. We acknowledge the NMDB database ([www.nmdb.eu](http://www.nmdb.eu)), funded under the European Union's FP7 Programme (contract 213007), for providing data. The data from South Pole neutron monitor is provided by the University of Delaware with support from the U.S. National Science Foundation under grant ANT0838839.

## References

- Amerstorfer, T., Möstl, C., Hess, P., Temmer, M., Mays, M. L., Reiss, M. A., ... Bourdin, P.-A. (2018). Ensemble prediction of a halo coronal mass ejection using heliospheric imagers. *Space Weather*, 16(7), 784-801. Retrieved from <https://agupubs.onlinelibrary.wiley.com/doi/abs/10.1029/2017SW001786> doi: 10.1029/2017SW001786
- Boteler, D., Pirjola, R., & Nevanlinna, H. (1998). The effects of geomagnetic disturbances on electrical systems at the earth's surface. *Advances in Space Research*, 22(1), 17 - 27. Retrieved from <http://www.sciencedirect.com/science/article/pii/S027311779701096X> (Solar-Terrestrial Relations: Predicting the Effects on the Near-Earth Environment) doi: [https://doi.org/10.1016/S0273-1177\(97\)01096-X](https://doi.org/10.1016/S0273-1177(97)01096-X)
- Cane, H. V. (2000). Coronal mass ejections and forrush decreases. *Space Science Reviews*, 93(1), 55-77. Retrieved from <http://dx.doi.org/10.1023/A:1026532125747> doi: 10.1023/A:1026532125747
- Cane, H. V., Richardson, I. G., & St. Cyr, O. C. (2000). Coronal mass ejections, interplanetary ejecta and geomagnetic storms. *Geophysical Research Letters*, 27(21), 3591-3594. Retrieved from <https://agupubs.onlinelibrary.wiley.com/doi/abs/10.1029/2000GL000111> doi: 10.1029/2000GL000111
- Cane, H. V., Richardson, I. G., & von Rosenvinge, T. T. (1996, October). Cosmic ray decreases: 1964-1994. *Journal of Geophysics Research*, 101, 21561-21572. doi: 10.1029/96JA01964
- Davies, J. A., Harrison, R. A., Perry, C. H., Möstl, C., Lugaz, N., Rollett, T., ... Savani, N. P. (2012). A self-similar expansion model for use in solar wind transient propagation studies. *The Astrophysical Journal*, 750(1), 23. Retrieved from <http://stacks.iop.org/0004-637X/750/i=1/a=23>
- Davies, J. A., Harrison, R. A., Rouillard, A. P., Sheeley Jr., N. R., Perry, C. H., Bewsher, D., ... Brown, D. S. (2009). A synoptic view of solar transient evolution in the inner heliosphere using the heliospheric imagers on stereo. *Geophysical Research Letters*, 36(2). Retrieved from <https://agupubs.onlinelibrary.wiley.com/doi/abs/10.1029/2008GL036182> doi: 10.1029/2008GL036182
- Dumbović, M., Vršnak, B., Čalogović, J., & Karlica, M. (2011, July). Cosmic ray modulation by solar wind disturbances. *Astronomy & Astrophysics*, 531, A91. doi: 10.1051/0004-6361/201016006
- Dumbović, M., Čalogović, J., Vršnak, B., Temmer, M., Mays, M. L., Veronig, A., & Piantchitsch, I. (2018). The drag-based ensemble model (dbem) for coronal mass ejection propagation. *The Astrophysical Journal*, 854(2), 180. Retrieved

- from <http://stacks.iop.org/0004-637X/854/i=2/a=180>
- Forbush, S. E. (1937, 6). On the effects in cosmic-ray intensity observed during the recent magnetic storm. *Phys. Rev.*, *51*, 1108–1109. Retrieved from <http://link.aps.org/doi/10.1103/PhysRev.51.1108.3> doi: 10.1103/PhysRev.51.1108.3
- Fox, N. J., Velli, M. C., Bale, S. D., Decker, R., Driesman, A., Howard, R. A., ... Szabo, A. (2016, 12 01). The solar probe plus mission: Humanity's first visit to our star. *Space Science Reviews*, *204*(1), 7–48. Retrieved from <https://doi.org/10.1007/s11214-015-0211-6> doi: 10.1007/s11214-015-0211-6
- Freiherr von Forstner, J. L., Guo, J., WimmerSchweingruber, R. F., Hassler, D. M., Temmer, M., Dumbovi, M., ... Zeitlin, C. J. (2018). Using forbush decreases to derive the transit time of icmes propagating from 1 au to mars. *Journal of Geophysical Research: Space Physics*, *123*(1), 39–56. Retrieved from <https://agupubs.onlinelibrary.wiley.com/doi/abs/10.1002/2017JA024700> doi: 10.1002/2017JA024700
- Gopalswamy, N., Davila, J., Cyr, O. S., Sittler, E., Auchère, F., Duvall Jr, T., ... others (2011). Earth-affecting solar causes observatory (easco): a potential international living with a star mission from sun–earth l5. *Journal of Atmospheric and Solar-Terrestrial Physics*, *73*(5-6), 658–663.
- Grotzinger, J. P., Crisp, J., Vasavada, A. R., Anderson, R. C., Baker, C. J., Barry, R., ... Wiens, R. C. (2012, 9 01). Mars science laboratory mission and science investigation. *Space Science Reviews*, *170*(1), 5–56. Retrieved from <https://doi.org/10.1007/s11214-012-9892-2> doi: 10.1007/s11214-012-9892-2
- Guo, J., Dumbovi, M., Wimmer-Schweingruber, R. F., Temmer, M., Lohf, H., Wang, Y., ... Posner, A. (2018). Modeling the evolution and propagation of 10 september 2017 cmes and seps arriving at mars constrained by remote sensing and in situ measurement. *Space Weather*, *16*(8), 1156–1169. Retrieved from <https://agupubs.onlinelibrary.wiley.com/doi/abs/10.1029/2018SW001973> doi: 10.1029/2018SW001973
- Guo, J., Lillis, R., Wimmer-Schweingruber, R. F., Zeitlin, C., Simonson, P., Rahmati, A., ... Böttcher, S. (2018). Measurements of forbush decreases at mars: both by msl on ground and by maven in orbit. *A&A*, *611*, A79. Retrieved from <https://doi.org/10.1051/0004-6361/201732087> doi: 10.1051/0004-6361/201732087
- Guo, J., Zeitlin, C., Wimmer-Schweingruber, R. F., Hassler, D. M., Posner, A., Heber, B., ... Reitz, G. (2015). Variations of dose rate observed by msl/rad in transit to mars. *A&A*, *577*, A58. Retrieved from <https://doi.org/10.1051/0004-6361/201525680> doi: 10.1051/0004-6361/201525680
- Guo, J., Zeitlin, C., Wimmer-Schweingruber, R. F., McDole, T., Khl, P., Appel, J. C., ... Köhler, J. (2018). A generalized approach to model the spectra and radiation dose rate of solar particle events on the surface of mars. *The Astronomical Journal*, *155*(1), 49. Retrieved from <http://stacks.iop.org/1538-3881/155/i=1/a=49>
- Hassler, D. M., Zeitlin, C., Wimmer-Schweingruber, R. F., Böttcher, S., Martin, C., Andrews, J., ... Cucinotta, F. A. (2012). The radiation assessment detector (rad) investigation. *Space Science Reviews*, *170*(1), 503–558. Retrieved from <http://dx.doi.org/10.1007/s11214-012-9913-1> doi: 10.1007/s11214-012-9913-1
- Heinemann, S. G., Temmer, M., Hofmeister, S. J., Veronig, A. M., & Vennerstrøm, S. (2018, July). Three-phase Evolution of a Coronal Hole. I. 360° Remote Sensing and In Situ Observations. *The Astrophysical Journal*, *861*, 151. doi: 10.3847/1538-4357/aac897
- Helcats, E., Barnes, D., Davies, J., & Harrison, R. (2018, Jan). *Helcats wp3 cme kinematics catalogue*. figshare. Retrieved from [https://figshare.com/articles/HELcats\\_WP3\\_CME\\_KINEMATICS\\_CATALOGUE/5803176/1](https://figshare.com/articles/HELcats_WP3_CME_KINEMATICS_CATALOGUE/5803176/1) doi:

- 10.6084/m9.figshare.5803176.v1
- Hess, V. F., & Demmelmair, A. (1937, 8). World-wide Effect in Cosmic Ray Intensity, as Observed during a Recent Magnetic Storm. *Nature*, 140, 316-317. doi: 10.1038/140316a0
- Howard, R. A., Moses, J. D., Vourlidas, A., Newmark, J. S., Socker, D. G., Plunkett, S. P., ... Carter, T. (2008, 5 16). Sun earth connection coronal and heliospheric investigation (secchi). *Space Science Reviews*, 136(1), 67. Retrieved from <https://doi.org/10.1007/s11214-008-9341-4> doi: 10.1007/s11214-008-9341-4
- Howard, R. A., Vourlidas, A., Korendyke, C. M., Plunkett, S. P., Carter, M. T., Wang, D., ... Lamy, P. L. (2013). The solar and heliospheric imager (solohi) instrument for the solar orbiter mission. *Proc.SPIE*, 8862, 8862. Retrieved from <https://doi.org/10.1117/12.2027657> doi: 10.1117/12.2027657
- Howard, T. A., Webb, D. F., Tappin, S. J., Mizuno, D. R., & Johnston, J. C. (2006). Tracking halo coronal mass ejections from 01 au and space weather forecasting using the solar mass ejection imager (smei). *Journal of Geophysical Research: Space Physics*, 111(A4), n/a-n/a. Retrieved from <http://dx.doi.org/10.1029/2005JA011349> (A04105) doi: 10.1029/2005JA011349
- Kahler, S. W., & Webb, D. F. (2007). V arc interplanetary coronal mass ejections observed with the solar mass ejection imager. *Journal of Geophysical Research: Space Physics*, 112(A9), n/a-n/a. Retrieved from <http://dx.doi.org/10.1029/2007JA012358> (A09103) doi: 10.1029/2007JA012358
- Kraft, S., Puschmann, K. G., & Luntama, J. P. (2017). Remote sensing optical instrumentation for enhanced space weather monitoring from the l1 and l5 lagrange points. *Proc.SPIE*, 10562, 10562. Retrieved from <https://doi.org/10.1117/12.2296100> doi: 10.1117/12.2296100
- Lavraud, B., Liu, Y. D., Segura, K., He, J., Qin, G., Temmer, M., ... Fernandez, J. (2016). A small mission concept to the sunearth lagrangian l5 point for innovative solar, heliospheric and space weather science. *Journal of Atmospheric and Solar-Terrestrial Physics*, 146, 171 - 185. Retrieved from <http://www.sciencedirect.com/science/article/pii/S1364682616301456> doi: <https://doi.org/10.1016/j.jastp.2016.06.004>
- Lefèvre, L., Vennerstrøm, S., Dumbović, M., Vršnak, B., Sudar, D., Arlt, R., ... Crosby, N. (2016, May). Detailed Analysis of Solar Data Related to Historical Extreme Geomagnetic Storms: 1868 - 2010. *Solar Physics*, 291, 1483-1531. doi: 10.1007/s11207-016-0892-3
- Liu, Y. D., Davies, J. A., Luhmann, J. G., Vourlidas, A., Bale, S. D., & Lin, R. P. (2010). Geometric triangulation of imaging observations to track coronal mass ejections continuously out to 1 au. *The Astrophysical Journal Letters*, 710(1), L82. Retrieved from <http://stacks.iop.org/2041-8205/710/i=1/a=L82>
- Liu, Y. D., Hu, H., Wang, C., Luhmann, J. G., Richardson, J. D., Yang, Z., & Wang, R. (2016). On sun-to-earth propagation of coronal mass ejections: II. slow events and comparison with others. *The Astrophysical Journal Supplement Series*, 222(2), 23. Retrieved from <http://stacks.iop.org/0067-0049/222/i=2/a=23>
- Liu, Y. D., Luhmann, J. G., Lugaz, N., Möstl, C., Davies, J. A., Bale, S. D., & Lin, R. P. (2013). On sun-to-earth propagation of coronal mass ejections. *The Astrophysical Journal*, 769(1), 45. Retrieved from <http://stacks.iop.org/0004-637X/769/i=1/a=45>
- Liu, Y. D., Thernisien, A., Luhmann, J. G., Vourlidas, A., Davies, J. A., Lin, R. P., & Bale, S. D. (2010). Reconstructing coronal mass ejections with coordinated imaging and in situ observations: Global structure, kinematics, and implications for space weather forecasting. *The Astrophysical Journal*, 722(2), 1762. Retrieved from <http://stacks.iop.org/0004-637X/722/i=2/a=1762>
- Lugaz, N., Hernandez-Charpak, J. N., Roussev, I. I., Davis, C. J., Vourlidas, A.,

- & Davies, J. A. (2010a). Determining the azimuthal properties of coronal mass ejections from multi-spacecraft remote-sensing observations with stereo secchi. *The Astrophysical Journal*, 715(1), 493. Retrieved from <http://stacks.iop.org/0004-637X/715/i=1/a=493>
- Lugaz, N., Hernandez-Charpak, J. N., Roussev, I. I., Davis, C. J., Vourlidas, A., & Davies, J. A. (2010b). Determining the azimuthal properties of coronal mass ejections from multi-spacecraft remote-sensing observations with stereo secchi. *The Astrophysical Journal*, 715(1), 493. Retrieved from <http://stacks.iop.org/0004-637X/715/i=1/a=493>
- Lugaz, N., Vourlidas, A., & Roussev, I. I. (2009). Deriving the radial distances of wide coronal mass ejections from elongation measurements in the heliosphere – application to cme-cme interaction. *Annales Geophysicae*, 27(9), 3479–3488. Retrieved from <https://www.ann-geophys.net/27/3479/2009/> doi: 10.5194/angeo-27-3479-2009
- Lugaz, N., Vourlidas, A., Roussev, I. I., & Morgan, H. (2009, May 01). Solar–terrestrial simulation in the stereo era: The 24–25 january 2007 eruptions. *Solar Physics*, 256(1), 269–284. Retrieved from <https://doi.org/10.1007/s11207-009-9339-4> doi: 10.1007/s11207-009-9339-4
- Müller, D., Marsden, R. G., St. Cyr, O. C., Gilbert, H. R., & The Solar Orbiter Team. (2013, 6 01). Solar orbiter. *Solar Physics*, 285(1), 25–70. Retrieved from <https://doi.org/10.1007/s11207-012-0085-7> doi: 10.1007/s11207-012-0085-7
- Möstl, C., Amla, K., Hall, J. R., Liewer, P. C., Jong, E. M. D., Colaninno, R. C., ... Galvin, A. B. (2014). Connecting speeds, directions and arrival times of 22 coronal mass ejections from the sun to 1 au. *The Astrophysical Journal*, 787(2), 119. Retrieved from <http://stacks.iop.org/0004-637X/787/i=2/a=119>
- Möstl, C., & Davies, J. A. (2013, 7 01). Speeds and arrival times of solar transients approximated by self-similar expanding circular fronts. *Solar Physics*, 285(1), 411–423. Retrieved from <https://doi.org/10.1007/s11207-012-9978-8> doi: 10.1007/s11207-012-9978-8
- Möstl, C., Isavnin, A., Boakes, P. D., Kilpua, E. K. J., Davies, J. A., Harrison, R. A., ... Zhang, T. L. (2017). Modeling observations of solar coronal mass ejections with heliospheric imagers verified with the heliophysics system observatory. *Space Weather*, 15(7), 955–970. Retrieved from <https://agupubs.onlinelibrary.wiley.com/doi/abs/10.1002/2017SW001614> doi: 10.1002/2017SW001614
- Möstl, C., Rollett, T., Frahm, R. A., Liu, Y. D., Long, D. M., Colaninno, R. C., ... Vršnak, B. (2015, May). Strong coronal channelling and interplanetary evolution of a solar storm up to Earth and Mars. *Nature Communications*, 6, 7135. doi: 10.1038/ncomms8135
- Möstl, C., Rollett, T., Lugaz, N., Farrugia, C. J., Davies, J. A., Temmer, M., ... Biernat, H. K. (2011). Arrival time calculation for interplanetary coronal mass ejections with circular fronts and application to stereo observations of the 2009 february 13 eruption. *The Astrophysical Journal*, 741(1), 34. Retrieved from <http://stacks.iop.org/0004-637X/741/i=1/a=34>
- Odstrcil, D., Riley, P., & Zhao, X. P. (2004). Numerical simulation of the 12 may 1997 interplanetary cme event. *Journal of Geophysical Research: Space Physics*, 109(A2), n/a–n/a. Retrieved from <http://dx.doi.org/10.1029/2003JA010135> (A02116) doi: 10.1029/2003JA010135
- Oughton, E. J., Skelton, A., Horne, R. B., Thomson, A. W. P., & Gaunt, C. T. (2017). Quantifying the daily economic impact of extreme space weather due to failure in electricity transmission infrastructure. *Space Weather*, 15(1), 65–83. Retrieved from <https://agupubs.onlinelibrary.wiley.com/doi/abs/10.1002/2016SW001491> doi: 10.1002/2016SW001491



- Pomoell, Jens, & Poedts, S. (2018). Euhforia: European heliospheric forecasting information asset. *J. Space Weather Space Clim.*, 8, A35. Retrieved from <https://doi.org/10.1051/swsc/2018020> doi: 10.1051/swsc/2018020
- Raffin, S. C. R., Zeitlin, C., Ehresmann, B., Hassler, D., Guo, J., Köhler, J., ... the MSL Science Team (2014). Diurnal variations of energetic particle radiation at the surface of mars as observed by the mars science laboratory radiation assessment detector. *Journal of Geophysical Research: Planets*, 119(6), 1345–1358. Retrieved from <http://dx.doi.org/10.1002/2013JE004525> doi: 10.1002/2013JE004525
- Reames, D. V. (2013, Jun 01). The two sources of solar energetic particles. *Space Science Reviews*, 175(1), 53–92. Retrieved from <https://doi.org/10.1007/s11214-013-9958-9> doi: 10.1007/s11214-013-9958-9
- Rollett, T., Möstl, C., Isavnin, A., Davies, J. A., Kubicka, M., Amerstorfer, U. V., & Harrison, R. A. (2016). Elevohi: A novel cme prediction tool for heliospheric imaging combining an elliptical front with drag-based model fitting. *The Astrophysical Journal*, 824(2), 131. Retrieved from <http://stacks.iop.org/0004-637X/824/i=2/a=131>
- Rouillard, A. P., Davies, J. A., Forsyth, R. J., Rees, A., Davis, C. J., Harrison, R. A., ... Perry, C. H. (2008). First imaging of corotating interaction regions using the stereo spacecraft. *Geophysical Research Letters*, 35(10). Retrieved from <https://agupubs.onlinelibrary.wiley.com/doi/abs/10.1029/2008GL033767> doi: 10.1029/2008GL033767
- Russell, C. T. (Ed.). (2008). *The STEREO mission*. Springer New York. Retrieved from <https://doi.org/10.1007/978-0-387-09649-0> doi: 10.1007/978-0-387-09649-0
- Sheeley, N. R., Walters, J. H., Wang, Y.-M., & Howard, R. A. (1999). Continuous tracking of coronal outflows: Two kinds of coronal mass ejections. *Journal of Geophysical Research: Space Physics*, 104(A11), 24739–24767. Retrieved from <https://agupubs.onlinelibrary.wiley.com/doi/abs/10.1029/1999JA900308> doi: 10.1029/1999JA900308
- Shen, C., Wang, Y., Wang, S., Liu, Y., Liu, R., Vourlidas, A., ... Zhou, Z. (2012, December). Super-elastic collision of large-scale magnetized plasmoids in the heliosphere. *Nature Physics*, 8, 923–928. doi: 10.1038/nphys2440
- Temmer, M., & Nitta, N. V. (2015, Mar 01). Interplanetary propagation behavior of the fast coronal mass ejection on 23 july 2012. *Solar Physics*, 290(3), 919–932. Retrieved from <https://doi.org/10.1007/s11207-014-0642-3> doi: 10.1007/s11207-014-0642-3
- Temmer, M., Vršnak, B., Rollett, T., Bein, B., de Koning, C. A., Liu, Y., ... Forsyth, R. (2012, mar). CHARACTERISTICS OF KINEMATICS OF a CORONAL MASS EJECTION DURING THE 2010 AUGUST 1 CME–CME INTERACTION EVENT. *The Astrophysical Journal*, 749(1), 57. Retrieved from <https://doi.org/10.1088/0004-637x/749/1/57> doi: 10.1088/0004-637x/749/1/57
- Tucker-Hood, K., Scott, C., Owens, M., Jackson, D., Barnard, L., Davies, J. A., ... Wan Wah, L. L. (2015). Validation of a priori cme arrival predictions made using real-time heliospheric imager observations. *Space Weather*, 13(1), 35–48. Retrieved from <https://agupubs.onlinelibrary.wiley.com/doi/abs/10.1002/2014SW001106> doi: 10.1002/2014SW001106
- Vennerstrøm, S., Lefevre, L., Dumbović, M., Crosby, N., Malandraki, O., Patsou, I., ... Moretto, T. (2016, May). Extreme Geomagnetic Storms - 1868 - 2010. *Solar Physics*, 291, 1447–1481. doi: 10.1007/s11207-016-0897-y
- Vourlidas, A. (2015). Mission to the sun-earth l5 lagrangian point: An optimal platform for space weather research. *Space Weather*, 13(4), 197–201.
- Vourlidas, A., Howard, R. A., Plunkett, S. P., Korendyke, C. M., Thernisien, A. F. R., Wang, D., ... Rodmann, J. (2016, 12 01). The wide-field im-



- ager for solar probe plus (wispr). *Space Science Reviews*, 204(1), 83–130. Retrieved from <https://doi.org/10.1007/s11214-014-0114-y> doi: 10.1007/s11214-014-0114-y
- Vršnak, B., Temmer, M., Žic, T., Taktakishvili, A., Dumbović, M., Möstl, C., ... Odstrčil, D. (2014). Heliospheric propagation of coronal mass ejections: Comparison of numerical wsa-enlil+cone model and analytical drag-based model. *The Astrophysical Journal Supplement Series*, 213(2), 21. Retrieved from <http://stacks.iop.org/0067-0049/213/i=2/a=21>
- Vršnak, B., Žic, T., Vrbanec, D., Temmer, M., Rollett, T., Möstl, C., ... Shanmugaraju, A. (2013). Propagation of interplanetary coronal mass ejections: The drag-based model. *Solar Physics*, 285(1), 295–315. Retrieved from <http://dx.doi.org/10.1007/s11207-012-0035-4> doi: 10.1007/s11207-012-0035-4
- Vršnak, B., & Žic, T. (2007). Transit times of interplanetary coronal mass ejections and the solar wind speed. *A&A*, 472(3), 937–943. Retrieved from <https://doi.org/10.1051/0004-6361:20077499> doi: 10.1051/0004-6361:20077499
- Wang, Y., Shen, C., Liu, R., Liu, J., Guo, J., Li, X., ... Zhang, T. (2018). Understanding the twist distribution inside magnetic flux ropes by anatomizing an interplanetary magnetic cloud. *Journal of Geophysical Research: Space Physics*, 123(5), 3238–3261. Retrieved from <https://agupubs.onlinelibrary.wiley.com/doi/abs/10.1002/2017JA024971> doi: 10.1002/2017JA024971
- Winslow, R. M., Schwadron, N. A., Lugaz, N., Guo, J., Joyce, C. J., Jordan, A. P., ... Mays, M. L. (2018, apr). Opening a window on ICME-driven GCR modulation in the inner solar system. *The Astrophysical Journal*, 856(2), 139. Retrieved from <https://doi.org/10.3847/2F1538-4357%2Faab098> doi: 10.3847/1538-4357/aab098
- Witasse, O., Snchez-Cano, B., Mays, M. L., Kajdi, P., Opgenoorth, H., Elliott, H. A., ... Altobelli, N. (2017). Interplanetary coronal mass ejection observed at stereo-a, mars, comet 67p/churyumov-gerasimenko, saturn, and new horizons en route to pluto: Comparison of its forbush decreases at 1.4, 3.1, and 9.9 au. *Journal of Geophysical Research: Space Physics*, 122(8), 7865–7890. Retrieved from <http://dx.doi.org/10.1002/2017JA023884> (2017JA023884) doi: 10.1002/2017JA023884
- Zeitlin, C., Hassler, D. M., Cucinotta, F. A., Ehresmann, B., Wimmer-Schweingruber, R. F., Brinza, D. E., ... Reitz, G. (2013). Measurements of energetic particle radiation in transit to mars on the mars science laboratory. *Science*, 340(6136), 1080–1084. Retrieved from <http://science.sciencemag.org/content/340/6136/1080> doi: 10.1126/science.1235989
- Zurbuchen, T. H., & Richardson, I. G. (2006). In-situ solar wind and magnetic field signatures of interplanetary coronal mass ejections. In *Coronal mass ejections* (pp. 31–43). New York, NY: Springer New York. Retrieved from [https://doi.org/10.1007/978-0-387-45088-9\\_3](https://doi.org/10.1007/978-0-387-45088-9_3) doi: 10.1007/978-0-387-45088-9\_3

Figure 1.

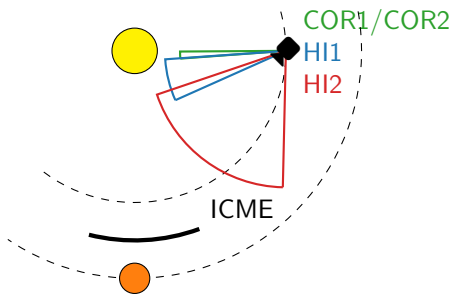
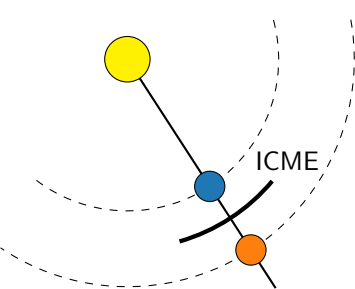
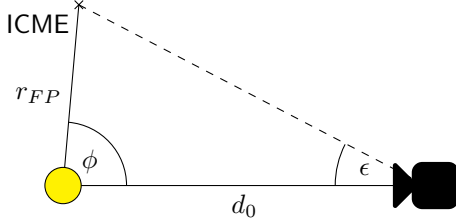
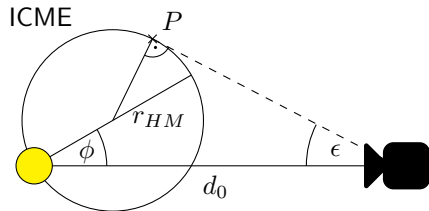


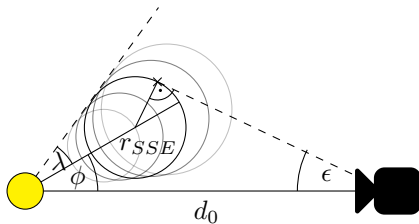
Figure 2.



**a) Fixed-Phi method**



**b) Harmonic mean method**



**c) Self-similar expansion method**

Figure 3.



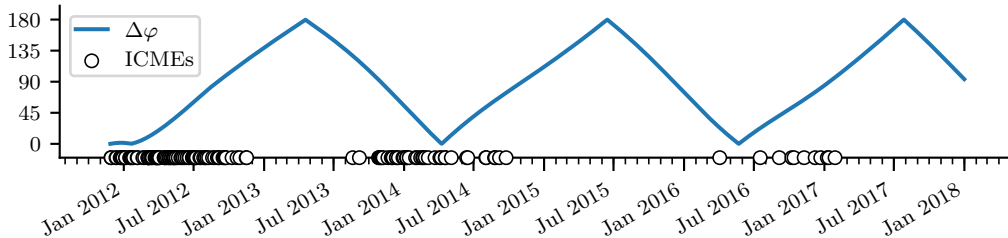


Figure 4.

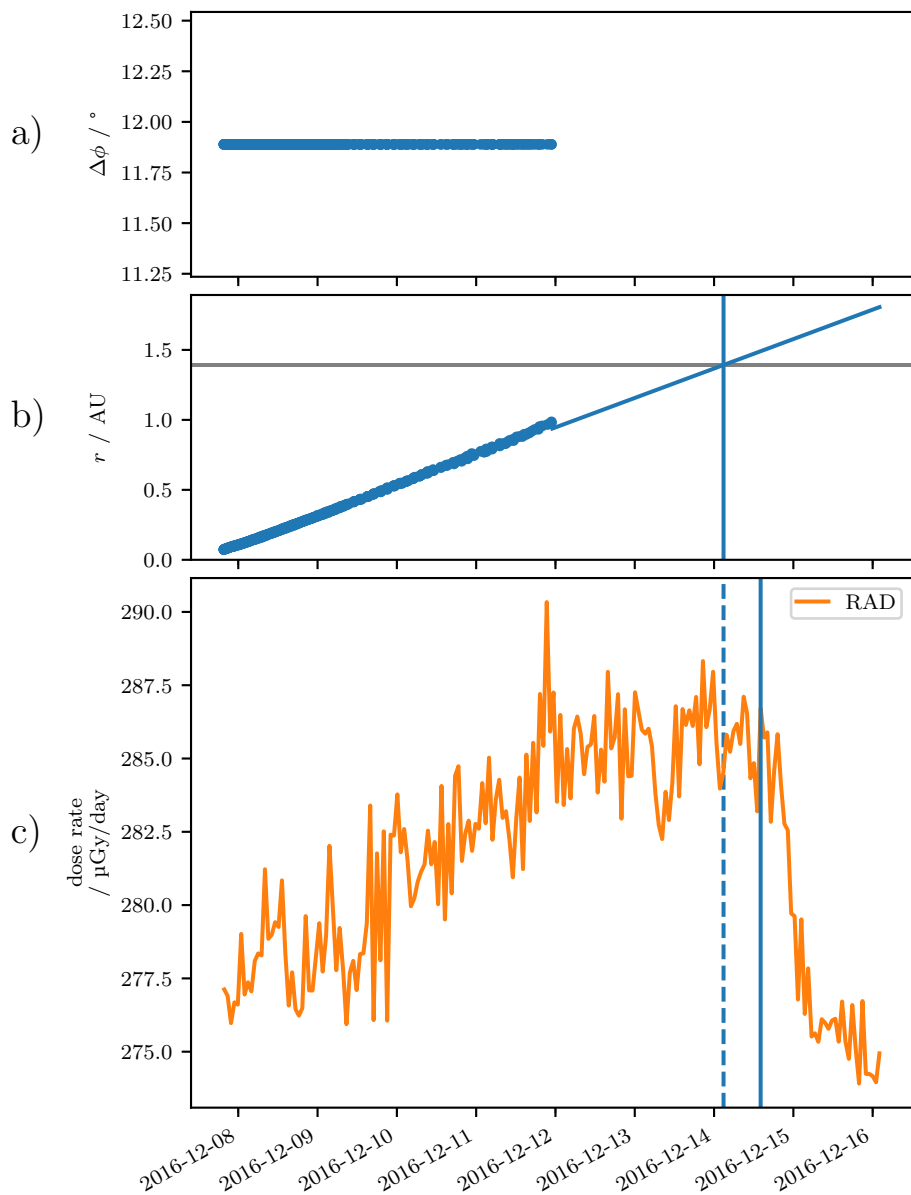
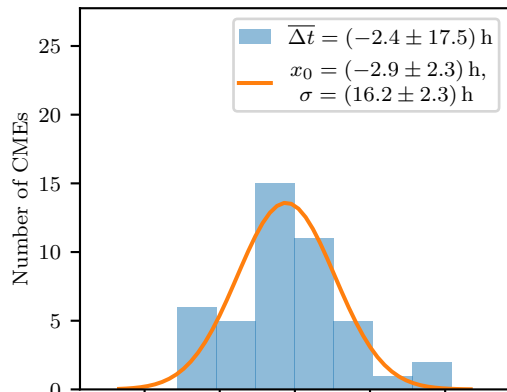
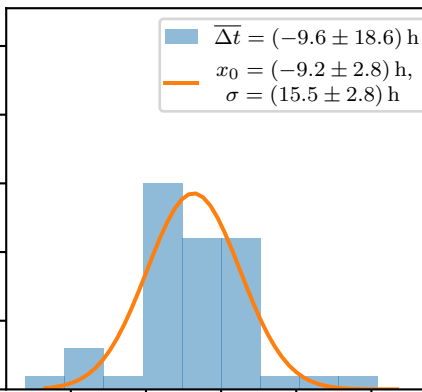


Figure 5.

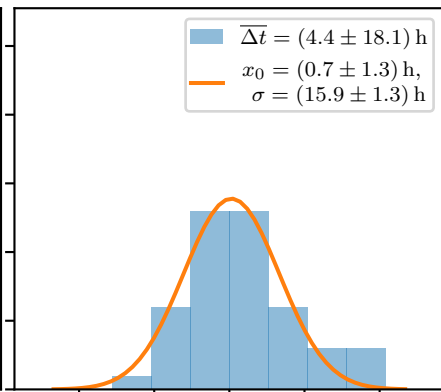
a) FP, Constant speed



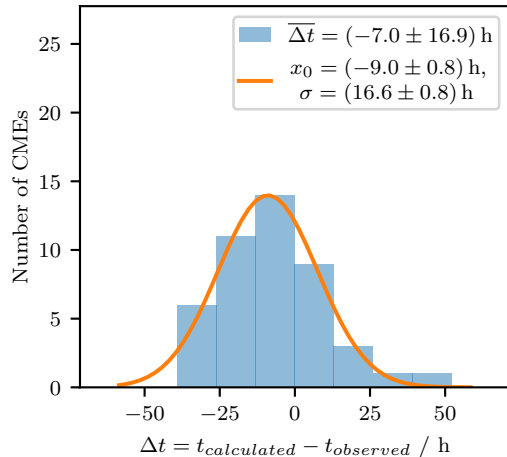
b) HM, Constant speed



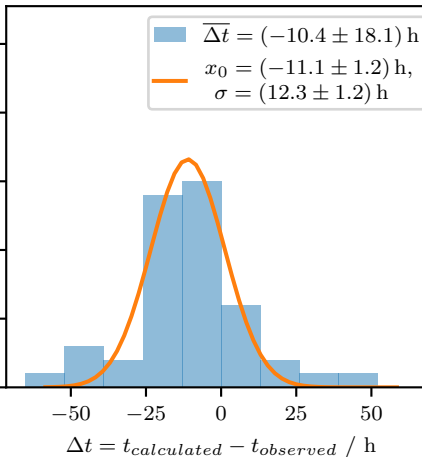
c) SSE, Constant speed



d) FP, Extrapolation



e) HM, Extrapolation



f) SSE, Extrapolation

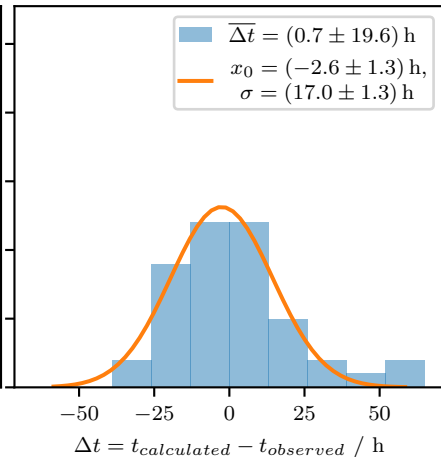


Figure 6.



